Journal of Materials Chemistry B

Accepted Manuscript

ROYAL SOCIETY OF CHEMISTRY

www.rsc.org/materialsB

Journal Name

RSCPublishing

ARTICLE

Directional Plk1 Inhibition-Driven Cell Cycle Interruption Using Amphiphilic Thin-Coated Peptide-Lanthanide Upconversion Nanomaterials as *in vivo* Tumor Suppressors

Cite this: DOI: 10.1039/x0xx00000x

Received 00th January 2012,
Accepted 00th January 2012

DOI: 10.1039/x0xx00000x

www.rsc.org/

Chi-Fai Chan[a], Rongfeng Lan[a], Ming-Kiu Tsang[e], Di Zhou[d], Sam Lear[c], Wai-Lun Chan[a], Steven L. Cobb*[c], Wai-Kwok Wong[a], Jianhua Hao[e], Wing-Tak Wong*[b,g], Ka-Leung Wong*[a,f]

Polo-like kinase 1 (Plk1) is a major serine/threonine protein kinase which regulates key mitotic events such as centrosome duplication, spindle assembly and chromosome separation. Overexpression and aberrant activities of Plk1 can be detected in various different types of cancer. Given that the unique polo box domain (PBD) pocket provides an excellent drug target for Plk1 binding and inhibition, we have rationally designed multifunctional lanthanide-doped upconverted nanomaterials. $NaGdF_4$: Yb^{3+}, Er^{3+} (**$NaGdF_4$**) and $BaGdF_5$: Yb^{3+}, Er^{3+}(**$BaGdF_5$**) nanoparticles of two different sizes (60 nm and 10 nm, respectively) have been thin-coated with Plk1 specific peptides (**-P_1** = PLHSpT, **-P_2** = PLHSD, and **-P_3** = GGPLHSpT) to prepare novel nanomaterials. Comparative studies looking at cellular uptake, anti-cancer activity and imaging properties were then carried out. The experimental data obtained supports our original hypotheses that the designed nanomaterials we prepared can successfully deliver Plk1 specific peptides into cancer cells causing Plk1 inhibition while simultaneously allowing direct NIR imaging and monitoring. From the **$NaGdF_4$–P_n** and **$BaGdF_5$-P_n** nanoparticle series prepared in this study, **$NaGdF_4$–P_1** emerged as the best candidate for Plk1 binding and imaging. **$NaGdF_4$–P_1** can effectively exert cell cycle G2/M arrest and thus selective tumor inhibition both *in vitro* and *in vivo* and as such it offers a potentially interesting system for the development of new cancer therapies.

1. Introduction

The human polo-like kinase family (Plk1-5) is responsible for a wide variety of cell regulatory activities such as DNA damage response, bipolar spindle formation, mitotic entry as well as cytokinesis[1-5]. However, the actual role of Plk1 in carcinogenesis is still yet to be to be fully elucidated. Some pre-clinical evidence suggests that overexpression of Plk1 is linked to an increased survival rate of cells[6], and this is supported by the fact that Plk1 normally highly expressed in actively proliferating tissue[7]. Strategic inactivation of Plk1 results in cell cycle arrest and subsequently apoptosis, thus Plk1 has emerged as a favorable therapeutic target for cancer treatment[8].

Within Plk1, there are two distinct domains — an amino-terminal kinase domain and a unique carboxyl terminal polo box domain (PBD). Several organic small molecules which can inhibit the Plk1 kinase domain and the PBD have been identified. Molecules such as BI2536, CBB2001 and MLN0905 target the kinase domain of Plk1 causing inhibition as well as pronounced dose-limiting toxicity (DLT)[9-11], however unspecific activities and unwanted side-effects have really limit the further development of Plk1 kinase domain targeting molecules. On the other hand, peptides and their analogues that can bind to the PBD present a novel and promising avenue for Plk1 targeting and inhibition[12-13].Peptides can be employed as tailor-made inhibitors and potential drugs but there are issues that working with this class of biological molecule presents. Peptides often display physical and chemical instabilities[14], poor cellular uptake, and localization issues[15]. Real-time assessments, including MTT, *in-vitro* imaging and tumor inhibition, are also crucial elements in cancer prognosis and treatment. Conventionally, for imaging purposes complex methods of analysis such as immunostaining using antibodies or fusion fluorescent proteins against Plk1 have been employed[16-17]. Recently, E. K. Ryu et al. demonstrated that a Plk1-specific peptide (PLHSpT) conjugated with the $\alpha_v\beta_3$ integrin receptor inhibitor peptide (RGD) and a radioligand can

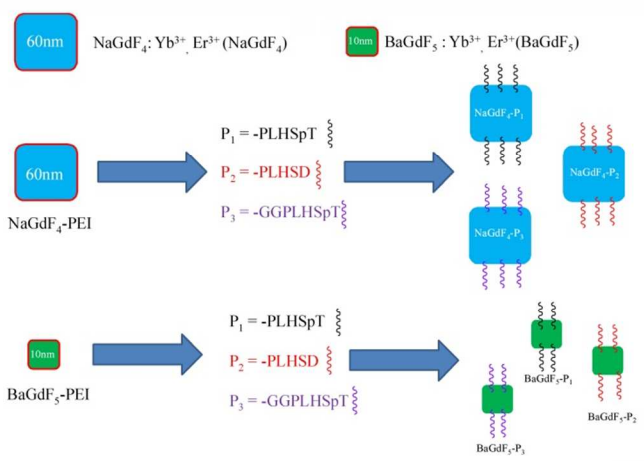

Figure 1. Schematic diagram of conjugating Plk1 specific peptides onto **$NaGdF_4$** and **$BaGdF_5$**.

achieve the much sought-after theranostic effect[14]. However, this is a rather indirect method of analysis and as it only tests cancer cells which involves multiple steps to interrupt the cell cycle, inhibit the tumor size, and diagnose the cancer tissues with PET. Most recently, we have reported a porphyrin-conjugated to a Plk1-specific peptide (e.g. PLHSpT) as a multi-modal bio-probe, with the molecular system serving as the vector[18]. The overall growth inhibition efficiency of it to the tumors through the singlet oxygen generation has, indeed, still room for further improvement.

In the present study we have prepared lanthanide-doped upconversion nanoparticles (UCNPs) which can act as a delivery vehicle for Plk1-specific peptides. The nano-particle-peptide conjugates were shown to inhibit Plk1 activity, while cell-cycle arrest and visualization can also be achieved simultaneously. Owing to the excellent photo-physical properties of lanthanide ions, the dopant ions (Ytterbium/ Erbium) can be excited and emit in the near-infrared (NIR) region. The nano-systems developed also offer additional benefits for bio-imaging such as improved light penetration depth, lower cytotoxicity and, above all, eliminated autofluorescence due to lanthanides' long emission lifetime (μs to ms) compared with that of organic biomarkers[19-28]. By conjugating the PBD binding peptide onto UCNPs, the cellular uptake problem of the individual peptides can also be addressed because the resulting organic-inorganic nanomaterial is highly biocompatible[29-30], and the peptides are protected from enzymatic degradation[31]. Although, in the case of cyclin D, the inhibitory effects of our previously established UCNPs ($NaGdF_4$: Yb^{3+}, Er^{3+}) conjugated with cyclin D-specific peptides was not as satisfactory as expected[32]. We have rationalized that this could be ascribed to unwanted cross bindings among various cyclins and their cyclin-dependent kinases (CDKs)[33], in addition, the *in-vitro* emission signal was also quenched after bio-conjugation when compared to the unmodified $NaGdF_4$: Yb^{3+}, Er^{3+}. With these factors in mind, we have now developed a new type of novel peptide-functionalized UCNPs which can achieve termination and visualization of cancer cells concurrently through binding and inhibition of Plk1.

Herein, we report the synthesis of eight UCNPs, using two solid systems of different sizes — 60 nm $NaGdF_4$: Yb^{3+}, Er^{3+} (**$NaGdF_4$**) and 10 nm $BaGdF_5$: Yb^{3+}, Er^{3+} (**$BaGdF_5$**). These two types of UCNPs are square, doped with Yb^{3+} and Er^{3+} at molar ratio 18:2 and coated with polyethyleneimine (**PEI**), PLHSpT (**P_1**)[13, 14], PLHSD (**P_2**) and GGPLHSpT (**P_3**) respectively. (Figure 1) All three peptides have already shown strong binding with PBD in Plk1[13]. **P_3**, which contained an additional Gly-Gly motif was used primarily to check whether any significant impact on the binding affinity between the peptide (i.e. PLHSpT) and Plk1, as well as the anti-tumor activity was observed when the linking distance between the UNCPs and the peptides was increased in length and flexibility. Comprehensive *in situ* (photophysical properties, protein pull down assay), *in vitro* (emission spectra, imaging, co-staining with GFP-Plk1, ICP-MS, cellular toxicity) and *in vivo* studies (imaging and solid tumor inhibition) in both cancer and normal cell lines have been conducted and the data is presented. Experimental results revealed that our 60 nm UNCPs have a better performance than the 10 nm UCNPs in terms of uptake efficiency and imaging quantity. In particular for **$NaGdF_4$-P_1** coated with the **P_1** peptides; control experiments have illustrated that **$NaGdF_4$-P_1** selective in its mode of action and it was demonstrated to have no anti-growth effect in the normal cells.

2. Results and discussion

Through conjugation to various inorganic molecules such as nanoparticles peptides can be effectively shielded from enzymatic degradation. In addition peptide coated UNCPs can be excited at 980 nm enabling real-time imaging to be carried out. In this stud, we intended to exploit both of these aforementioned properties coupled with Plk1 targeting to design and prepare nanosystems capable of simultaneous Plk1 inactivation and real time imaging, something that is not currently easily achievable. Two sets of UNCPs of differing sizes have been conjugated with three kinds of Plk1 specific peptides and photophysical properties, cellular uptake efficiency, *in vitro* imaging and selectivity for Plk1 of these systems have been evaluated. The UCNPs have been characterized and verified by a series of experiments including spectroscopic measurements, microscopic analyses and competitive assays through protein binding and western blotting. In addition to investigating a selection of Plk1 specific peptides and different UCNPs, we also wished to probe the effects of the size and shape of UCNPs themselves. Thus we used 60 nm and 10 nm UCNPs as both of them have similar crystal lattice and they are square in shape. Through this comprehensive study, we aimed to satisfy our hypothesis that Plk1 specific coated nanomaterials can act as promising systems in the future development of multi-modal anti-cancer upconversion nano-drugs.

2.1 Synthesis and characterization of nanoparticles conjugated with Plk1 (P_n) specific peptides

The surface groups of our **$NaGdF_4$** and **$BaGdF_5$** were examined by FTIR. The corresponding IR transmission spectrum of amine-functionalized **$NaGdF_4$** and **$BaGdF_5$** is shown in Figure S1. The broad absorption band centered at 3459 cm^{-1} is due to the O-H / N-H stretching vibration. The IR absorption peaks at 1637 and 1436 cm^{-1} are attributable to the N-H bending of the amino group (NH_2) and the C-N bond stretching vibration. Therefore, the IR transmission spectrum fully supports the capping of poly(ethyleneimine) (PEI) on the surface of **$NaGdF_4$** and **$BaGdF_5$**. The amine-functionalized

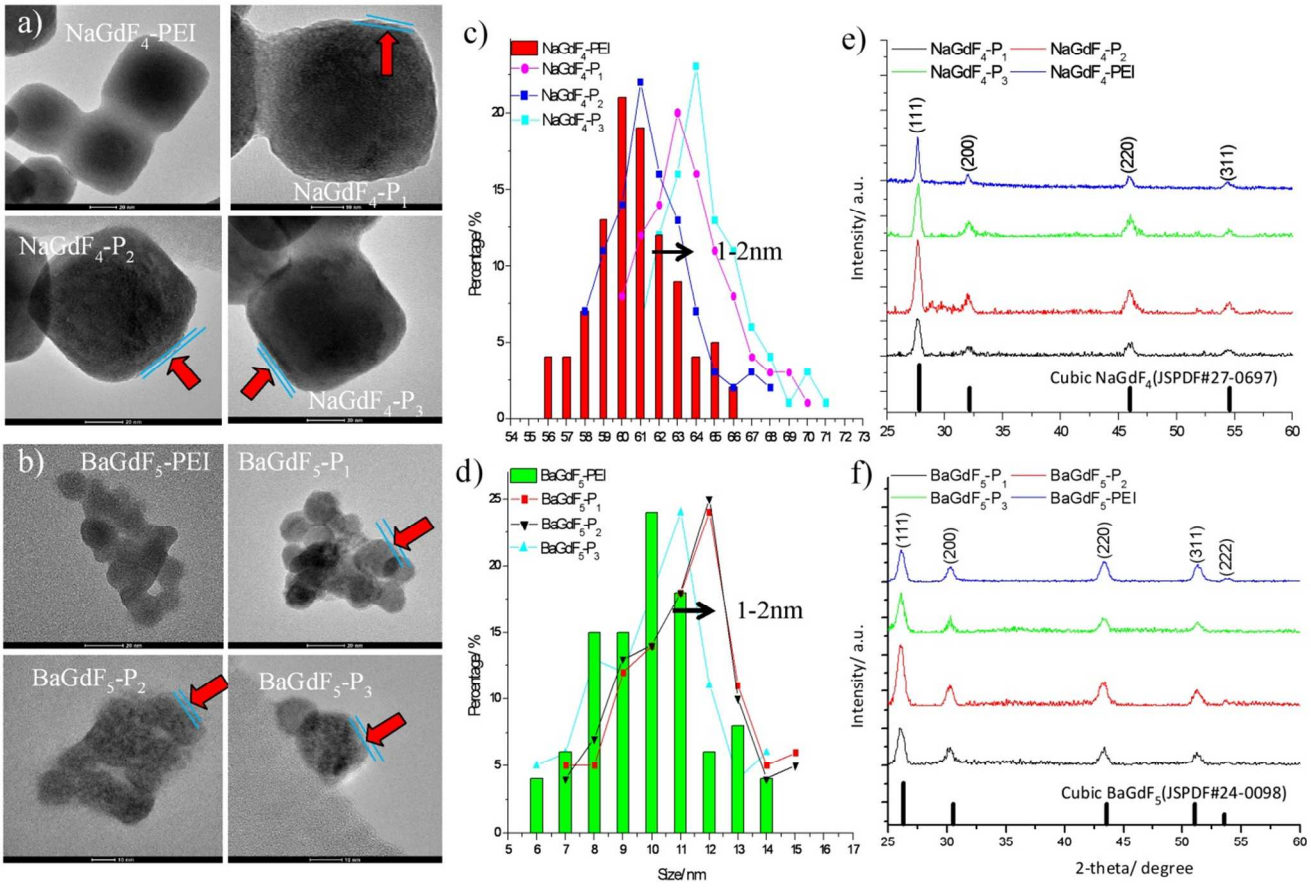

Figure 2. Surface characterization by (a)-(b) TEM analysis; (c)-(d) Size distribution and (e)-(f) XRD pattern analysis

$NaGdF_4$ and **$BaGdF_5$** were then modified into amide-functionalized **$NaGdF_4$–ene** and **$BaGdF_5$–ene**. The conversion of amine to amide was verified by the IR spectrum in Figure S1(b). The overall spectrum is similar to Figure S1(a). In fact, the absorption peaks at 1648 cm^{-1} newly appear under the stretching vibration of the C=O bond[34]. Figure S1(c) shows the IR spectrum recorded addition of the target specific peptide **P_n** on the surface of **$NaGdF_4$** and **$BaGdF_5$**. The small absorption peaks around 3022 to 3417 cm^{-1} represent the N-H bond stretching while the broad peak at 3307 cm^{-1} stands for the carboxylic acid. Hence, we had confirmed the successful coating of target specific peptide **P_n** onto our **$NaGdF_4$** and **$BaGdF_5$**.

The shape and morphology of **$NaGdF_4$**or **$BaGdF_5$** and peptide coated **$NaGdF_4$–P_n** or **$BaGdF_5$-P_n**, on the other hand, were investigated by TEM. In Figure 2a and 2b, the morphology of **$NaGdF_4$** and **$BaGdF_5$** was square in shape which corresponds to the cubic phase of **$NaGdF_4$** and **$BaGdF_5$**. This observation is similar to the previously reported synthesis of the cubic phase **$NaGdF_4$** [30] and **$BaGdF_5$** [35] which were verified by the SAED pattern of **$NaGdF_4$** and **$BaGdF_5$** as shown in Figure S2. From the high resolution TEM (HRTEM), a thin layer is observed (as indicated by red arrow) and the size distribution in TEM images reveal also that the overall sizes of Plk1 specific peptide coated **$NaGdF_4$-P_n** and **$BaGdF_5$-P_n** increase by 1-2 nm compared with the bare **$NaGdF_4$** and **$BaGdF_5$**, thereby justifying the conjugation of **$NaGdF_4$** and **$BaGdF_5$** with peptide **P_n**. As demonstrated by the dynamic light scattering analysis, the size of the nanomaterials is also increased by 1-3 nm after the peptide conjugation. (Figure S5) Besides, the surface charges of **$NaGdF_4$** and **$BaGdF_5$** should be different before and after the peptide conjugation. In Figure 3, there is clearly a drop of zeta potential which again qualifies the successful peptide conjugation onto our nanomaterials.

The phase composition of **$NaGdF_4$** or **$BaGdF_5$** and peptide coated **$NaGdF_4$ -P_n** or **$BaGdF_5$-P_n** was revealed by powder X-ray diffraction (XRD). In Figure 2e and 2f, the **$NaGdF_4$** and **$BaGdF_5$**, were indexed to the standard cubic phase **$NaGdF_4$** (JSPDF#27-0697) and **$BaGdF_5$** (JSPDF#24-0098) respectively. The diffraction peaks agree well with the standard pattern, with the matching result indicating that our **$NaGdF_4$** and **$BaGdF_5$** present in pure cubic phase with no other phase impurities. After the coating of Plk1 specific peptides on the surface of **$NaGdF_4$-P_n** or **$BaGdF_5$-P_n**, the XRD patterns show no changes in the 2-theta angles and this implies that the coating of peptide did not induce changes in crystal structure of both **$NaGdF_4$** and **$BaGdF_5$**. Also, this observation was consistent with the non-crystalline nature of peptide.

2.2 Photophysical properties of upconversion nanoparticles

In Yb^{3+} and Er^{3+} co-doped nanoparticles, under 980 nm laser diode excitation, Yb^{3+} ions possessing a large absorption cross section, much longer excited state lifetime and the energy ($^2F_{5/2}$→$^2F_{7/2}$) well resonant with higher-energy states of other

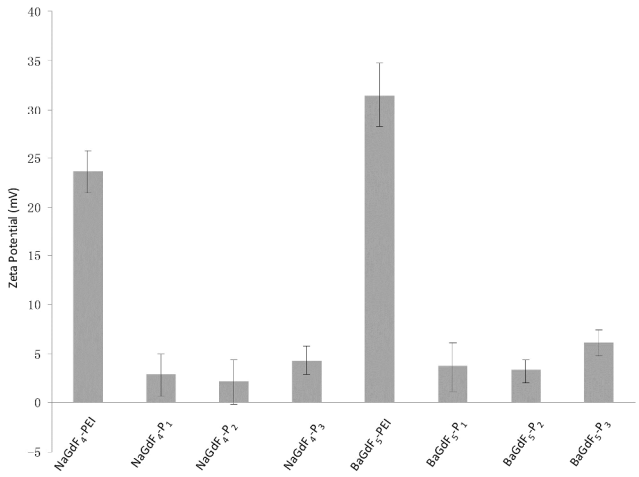

Figure 3. Peptide conjugation leads to a drop of zeta potential since peptides are relatively more negative compared with the PEI on $NaGdF_4$ or $BaGdF_5$.

lanthanide ions, can transfer energy continuously and efficiently to Er^{3+} ions, leading to bright upconversion luminescence in the visible region. Figure 4 shows the emission spectra of the peptide coated **$NaGdF_4$** and **$BaGdF_5$** (NPs), as well as the spectra of all the coated NPs indicating the same structures. The three emission peaks at 521 nm, 541 nm, and 650 nm arise from $^2H_{11/2} \rightarrow {}^4I_{15/2}$, $^4S_{3/2} \rightarrow {}^4I_{15/2}$, and $^4F_{9/2} \rightarrow {}^4I_{15/2}$ transitions respectively, which are ascribed to the two-photon upconversion process under 980 nm excitation with 340 mW and commonly present in nanomaterials doped with Yb^{3+} and Er^{3+} ions. The nearby peaks are originated from transitions between other Stark levels of the corresponding excited energy levels and the ground state. In order to understand the upconversion mechanism well, we measured the decay time curves for the peptide coated UCNPs. The insets of Figure 4a and b display the luminescence decay curves of $^4S_{3/2} \rightarrow {}^4I_{15/2}$ transition of Er^{3+} ions in **$NaGdF_4$-P_n** and **$BaGdF_5$-P_n**. Each of the down edges of the decay curves can be fitted well into a single exponentials function $I(t) = I_0 \exp(-t/\tau)$, where I_0 is the initial emission intensity at $t = 0$, and τ is decay time. The lifetime for the 541 nm emission peak is ~30 μs. Moreover, all the decay curves consist of rising edges, indicating that the population of $^4S_{3/2}$ originates from the energy transfer of the sensitizer Yb^{3+} ions. The upper level $^4F_{7/2}$ was populated by two-step upconversion energy transfer of Yb^{3+} ions and then nonradiatively relaxed to $^4S_{3/2}$, which resulted in the 541 nm emission. Thus the population of $^4S_{3/2}$ level is closely related to the phonon state density and the emission would be sensitive to the temperature. From Figure 4a, the nanoparticles of **$NaGdF_4$** coated with different peptides show remarkably different emission intensities, thereby implying the obvious influences of the surface coating to the upconversion properties of the nanoparticles. In short, the peptide coated nanoparticles emitting a long lifetime bright visible light under near infrared excitation could be an ideal material to achieve termination and visualization of cancer cell simultaneously.

2.3 *In vitro* cell based assay of UCNPs.

The application of peptides as potential anti-cancer agents is not a new concept; but, there are very limited methods for probing directly the uptake of such peptides *in vitro*. In our system, the lanthanide content in peptide-functionalized UCNPs offers an in built and direct monitoring opportunity for ICP-MS evaluation of peptide uptake efficiency *in vitro*. (Figure 5) From the analysis of the ICP-MS results (Figure 5), it can be seen that the uptake of two unfunctionalized nanoparticles are similar in both the cancer (HeLa) and the normal (liver derived QSG-7701) cells lines. A variation in the uptake rate occurs when the UNCPs are coated with peptides, especially peptide **P_1** and peptide **P_3**. (see arrows in Figure 5) In fact, in general, there are three main differences between peptide coated and unfunctionalized UCNPs. Firstly, coating with peptides facilitates cell permeability in both cancer (HeLa) and normal (liver derived QSG-7701) cells. Secondly, the 60 nm **$NaGdF_4$-P_n** shows slightly higher cellular uptake efficiency in comparison with 10 nm **$BaGdF_5$-P_n** in both cancer and normal cell lines. The underlying reason for this could simply be that in the 60 nm systems a larger the surface area is available, and thus more peptides are coated on the nanoparticle. Lastly, peptides **P_1** and **P_3** helped improve the selectivity of the uptake, mostly possibly due to the hydrophilic peptides enhanced the distribution of nanoparticles. In addition, cellular Plk1 may also increase nanoparticles accumulation through specific peptide-protein binding (i.e. greater difference between uptake into cancer versus normal cells). From this later point it also appears that specific sequence of the peptides, but not their actual length, that is important in the binding interactions with Plk1.

Given that our nanomaterials demonstrated interesting photo-physical properties within the biological window, high selectivity for Plk1 (by western blotting), and that they are more ready taken up by cancer cells, the potential of **$NaGdF_4$-P_n** or **$BaGdF_5$-P_n** to act as *in vitro* imaging bio-probes for Plk1 appeared very promising. To investigate this further, *in vitro* experiments were conducted in cervical carcinoma HeLa cells with two-photon microscopes. (Figure S3) **$NaGdF_4$-P_n** or **$BaGdF_5$-P_n** have, as expected, detectable emissions within the biological window (500 nm to 700 nm) via the near-infrared excitation at 980 nm. Such upconversion inside the cells can also help us to confirm the cell permeability of our UCNPs. The near-infrared (excitation) to near-infrared (emission) *in vitro* imaging of **$NaGdF_4$-P_n**or **$BaGdF_5$-P_n** can be correlated to the uptake results in Figure S3. Under the NIR excitation by the multi-photon confocal microscope, the impressive green ($^4S_{3/2} \rightarrow {}^4I_{15/2}$) and red (Figure 6, $^2F_{9/2} \rightarrow {}^4I_{15/2}$) f-f emission can be observed in HeLa cells due to the presence of **$NaGdF_4$-P_n** or **$BaGdF_5$-P_n** after 24 hours incubations. The *in vitro* emission spectra were recorded with the lambda scan system in the confocal microscope (resolution = 3 nm), the erbium emission bands $^4S_{3/2} \rightarrow {}^4I_{15/2}$ and $^2F_{9/2} \rightarrow {}^4I_{15/2}$ are found which is the same as our measurements with these **UCNP-P_n** in aqueous solution. Obviously, the *in vitro* emission of 60 nm **$NaGdF_4$-P_n** is far more intense than the 10 nm**$BaGdF_5$-P_n** *in vitro*. This observation can be found from the *in vitro* imaging and its emission spectra. **$NaGdF_4$-P_1** and **$NaGdF_4$-P_3** show impressive red emission inside the cell.

The selectivity of the UCNPs prepared toward Plk1 binding was confirmed by co-staining experiments with GFP-Plk1 specific fluorescent protein. (GFP-Plk1 protein is not available with the excitation at 980 nm). The co-staining experiments were carried out with the transient expression of the GFP-Plk1 protein in the cancer cells through plasmid transfection, followed by incubation with the UCNPs for another 24 hours. In the Figure 6a, the red emission from bare **$NaGdF_4$** (λ_{ex} = 980

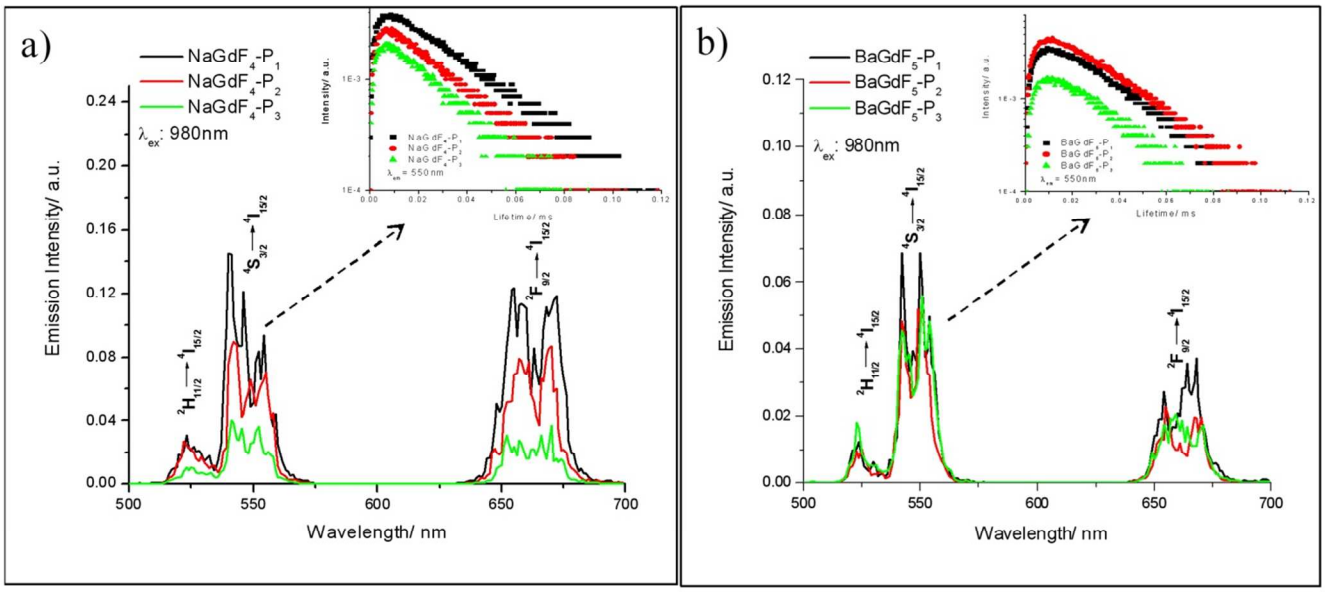

Figure 4. Upconversion emission spectra of (a) **$NaGdF_4$-P_n** and (b) **$BaGdF_5$-P_n** .The insets are their corresponding lifetime at λ_{em}: 541nm.

nm) is not overlapped with the green emission from GFP-Plk1 protein (λ_{ex}= 488 nm). However, in Figure 6b and 6d, the red emission from **$NaGdF_4$–P_1** and **$NaGdF_4$–P_3** overlapped with the green emission from GFP-Plk1 well. (Red circle and white arrow in Figure 6b and 6d). From the *in vitro* microscope, the up-conversion spectra showing the uptake behaviours of those nanomaterials are similar to what we found in ICP-MS uptake assays. The up-conversion red emission from **$NaGdF_4$-P_1**and **$NaGdF_4$-P_3** can be overlayed with the green GFP emission, further supporting the nano-materials selectivity towards Plk1. In order to further verify the binding selectivity of **$NaGdF_4$-P_n** or **$BaGdF_5$-P_n** towards Plk1, the nanoparticle-peptides bound Plk1 proteins performed by pull down assay in total cell lysate were examined using anti-Plk1 antibodies and western blotting. Among the various **$NaGdF_4$-P_n** or **$BaGdF_5$-P_n** tested, the **$NaGdF_4$-P_1** show the highest binding affinity towards Plk1 (about 10-fold higher) as revealed by the graph of relative Plk1 intensity (Figure 6m and 6n). Therefore, we propose that by conjugating the Plk1 specific peptide **P_1** onto the surface, the cellular uptake of our **UCNPs** should be much higher rather than conjugating other peptides (**P_2** and **P_3**). Hence, **$NaGdF_4$-P_1** is the best candidate functioning as *in vivo* imaging nanomaterial compared with the other Plk1 specific peptide analogues.

2.4 Inhibition of cell viability and cancer cell cycle interruption

Plk1 expression in different kinds of tumor cells is higher than compared with normal healthy cells. Therefore, before further studies and applications could be investigated, the inhibition effect of **$NaGdF_4$-P_n** or **$BaGdF_5$-P_n** in cancer cell had to be investigated. Firstly, cell viability was examined using an MTT assay in various cell lines (details given in the experimental section). Cell inhibition rates were calculated via viability related absorbance. In Figure 7, **$NaGdF_4$-P_n** or **$BaGdF_5$-P_n** exerted inhibition effect on cell viability, in comparison with the results using **$NaGdF_4$ –PEI** and **$BaGdF_5$ –PEI** in tested cell lines. Among the different Plk1 specific peptides conjugated to the **$NaGdF_4$-P_n** or **$BaGdF_5$-P_n** systems, **$NaGdF_4$-P_n**, showed better inhibition in the cancer (HeLa and HK-1) cells in contrast to **$BaGdF_5$-P_n** as highlighted in Figure 7. The results from the MTT assays carried out in normal cell lines, namely MRC-5 and QSG-7701, demonstrated the selectivity of **$NaGdF_4$-P_n** or **$BaGdF_5$-P_n** towards cancer cell lines (which over-express Plk1). In fact, there is a comparable amount of as-prepared nanoparticles up-taken by HeLa cells and QSG-7701 cells but the inhibition effect in HeLa is much higher than that of QSG-7701, thereby proving that our **$NaGdF_4$-P_n** or **$BaGdF_5$-P_n** can selectively kill cancer cells but remained relatively non-toxic to the normal cells. The IC_{50} values of

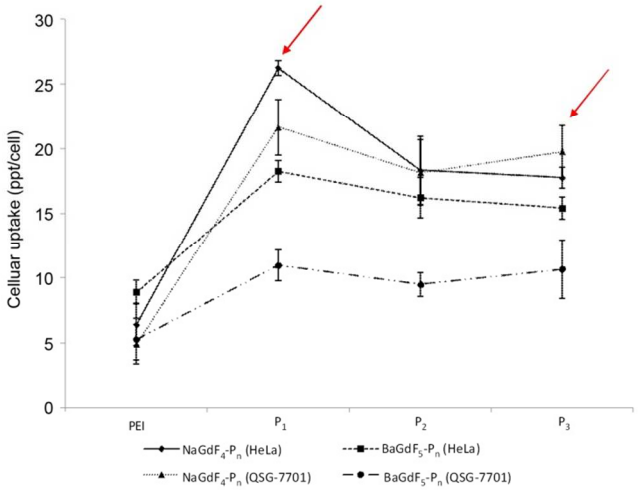

Figure 5. HeLa and QSG-7701 cellular uptake profile of **$NaGdF_4$-P_n** and **$BaGdF_5$-P_n** by ICP-MS. The y-axis is the cellular uptake concentration in ppt level per cell.

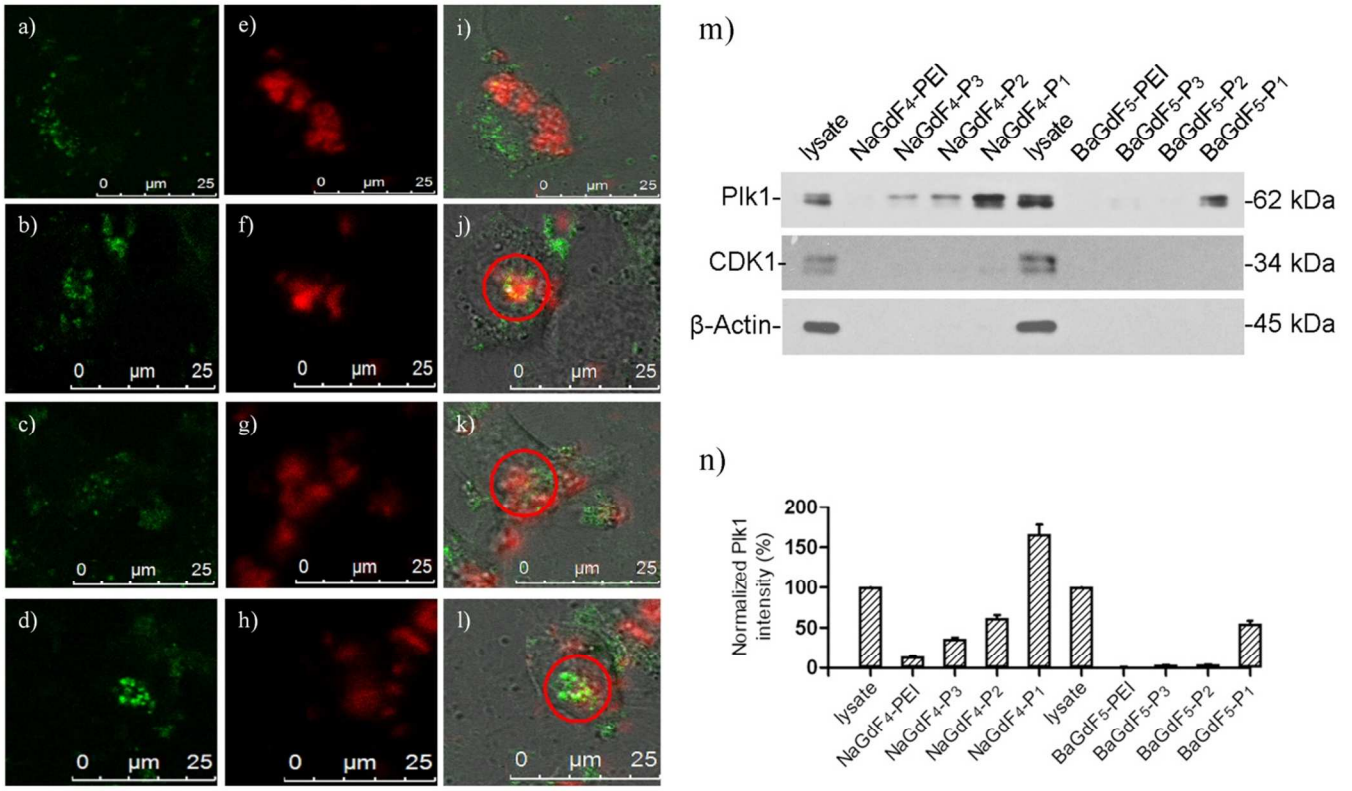

Figure 6.*In-vitro* images of (a)-(d) expressed GFP-Plk1; (e)-(h) upconversion emission of **$NaGdF_4$-PEI**, **-P_1**, **-P_2**, **-P_3** respectively and (i)-(l) their overlay images in HeLa cells. (m), (n) The pull down assay compared the binding affinity among **$NaGdF_4$-P_n** or **$BaGdF_5$-P_n** towards Plk1 and their relative Plk1 intensity respectively.

$NaGdF_4$-P_n or **$BaGdF_5$-P_n** are provided in the supporting information Table S1. Furthermore, cell cycle interruption was evaluated by flow cytometry. All of the Plk1 specific peptide coated **$NaGdF_4$-P_n** or **$BaGdF_5$-P_n** (0-100 μg/mL) and control (**$NaGdF_4$-PEI** or **$BaGdF_5$-PEI**) had been tested for the inhibition activity and the data are shown in Figure 7e. Normally, the cell phase distribution of usual cell division is ~67%, ~10% and ~23% in G1, G2 and S phases respectively. However, when treated with various **$NaGdF_4$-P_n** or **$BaGdF_5$-P_n**, only the **$NaGdF_4$-P_1** showed a significant G2 phase arrest at the dosage concentration of 100 μg/mL (indicated with statistic significance) while other **$NaGdF_4$-P_n** or **$BaGdF_5$-P_n** showed milder cell cycle interruption.

2.5 *In vivo* bio-distribution and mouse xenograft tumor inhibition.

In order to study the metabolism of **$NaGdF_4$-P_n** or **$BaGdF_5$-P_n** in an animal model, gadolinium concentration in different mouse tissues were analyzed with ICP-MS. Figure 8a to 8c, show that **$NaGdF_4$-PEI** and **$NaGdF_4$-P_1** accumulate in mice spleen and liver 6 hours after caudal vein injection, while **$BaGdF_5$-PEI** shows low accumulation in these organs. The reason for this is that **$BaGdF_5$-PEI** was quickly metabolized and excluded. Since liver and spleen are the primary organs responsible for detoxification, our nano-materials were captured and residue in these organs. Interestingly, compared with **$NaGdF_4$-PEI**, **$NaGdF_4$-P_1** not only accumulates in the spleen and liver, but it is also excreted in high concentration in the urine which suggests a longer retention time in the body. (Figure 8a and 8c) In addition, mouse xenograft tumor inhibition was also investigated using our nano-materials which were subcutaneous injected around the tumor. Figure 8d clearly shows that treatment with **$NaGdF_4$-P_n** (especially **$NaGdF_4$-P_1**) results in tumor shrinkage while **$BaGdF_5$-P_n** shows only a slight effect on the tumor. Therefore, the tumor inhibition performance of the **$NaGdF_4$-P_n**systems was better than that of the **$BaGdF_4$-P_n**systems which is completely in line with the results arising from the *in vitro* cell line based inhibition studies.

3. Experimental

3.1 Chemicals and Materials

$Ln(NO_3)_3.6H_2O$ (Ln = Gd, Yb, Er) were purchased from Aldrich and dissolved in de-ionized water (DI-water) to form solutions with concentrations of 0.5 M and 0.1 M. acrylic acid, Triisopropylsilane (TIS) and N-Hydroxy-succinimide (NHS, 98%) were purchased from Aldrich. Ethylene glycol (EG, 99%), branched polyethylenimine (PEI, 25 kDa), $BaCl_2$ (99.99%) and Trifluoroacetic acid (TFA, 99%) and were purchased from Sigma-Aldrich. NH_4F (99.99%) and NaCl (99.99%) were obtained from Sinopharm Chemical Reagent Co., China., N,N'-Dicyclohexylcarbodiimide (DCC, 99%) were purchased from Meryer. 3-(tritylthio)propanoic acid (>99%) was purchased from Dieckmann. All of these chemicals were used as received without further purification.

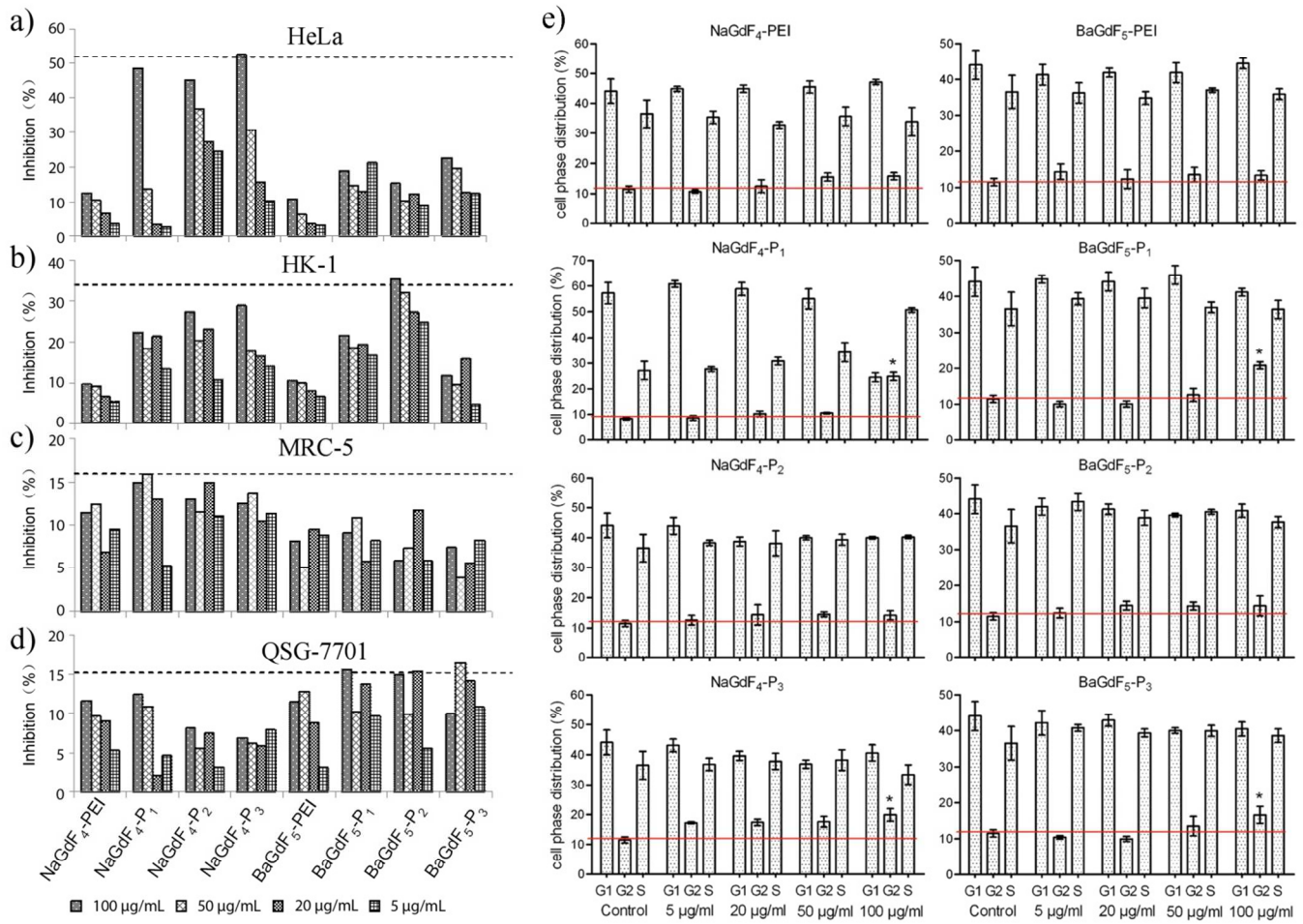

Figure 7. MTT inhibition assays of **$NaGdF_4$-P_n** and **$BaGdF_5$-P_n** in (a) Human cervical cancer HeLa; (b) Human nasopharyngeal carcinoma HK-1; (c) Human normal lung fibroblast MRC-5 cell; (d) Human liver-derived QSG-7701 cell, and (e) Cell cycle interruption in HeLa with flow cytometric analysis. * represent the statistic significance of $P< 0.01$

3.2 Synthesis of $NaGdF_4$ and $BaGdF_5$ upconversion nanoparticles

Water-dispersed **$NaGdF_4$**was prepared by one-step hydrothermal method. Typically, 1 mmol of NaCl and 1 mmol of $Gd(NO_3)_3$ (0.5 M), $Yb(NO_3)_3$ (0.5 M) and $Er(NO_3)_3$ (0.1 M) with the molar ratio of 78 : 20 : 2 were dissolved in 20 mL of ethylene glycol (EG) and stirred for 30 min. After capping with polyethyleneimine (PEI, branched 25kDa), approximately 10 mL of EG containing 5.5 mmol of NH_4F was then added to above solution and stirred for another 30 min. The obtained mixture was then transferred into a 50 mL stainless Teflon-lined autoclave, which was sealed and kept at 190˚C for 24 h. After that, the autoclave was cooled to room temperature naturally and the reaction mixture was separated through centrifugation. Ethanol and DI-water were used to wash the precipitation for several times and dried at 70˚C for 12 h to obtain the as-prepared samples. As a result, **$NaGdF_4$** with PEI as the surface modifier was prepared by hydrothermal method. The synthesis of **$BaGdF_5$** are similar to the above procedure but replaced the NaCl with $BaCl_2$. The zeta-potential for the **$NaGdF_4$** or **$BaGdF_5$** colloidal solution was measured to be around +23.6mV and +31.5mV respectively, indicating the successful conjugation of positively charged PEI on the surface of NPs.

3.3 Synthesis of Plk1 specific peptides

The three peptides were obtained by stepwise elongation of the peptide chain by the method outlined below. For peptide **P_1**, 500mg of the rink amide resin (0.45 mmol/g loading) was suspended in a 20% solution of piperidine in DMF, stirred for 20 min at room temperature and washed with DMF prior to subsequent steps. The first amino acid to be coupled, Fmoc-(Bn-p)-Thr-OH (420mg, 4 equiv) was dissolved in DMF and coupled to the resin in the presence of PyBOP (645mg, 4 equiv) and NMM (135 μL, 4 equiv) with the use of microwave chemistry as described previously.[15, 32] Other Fmoc amino acid derivatives: Fmoc-Ser(^{t}Bu)-OH (420mg, 4 equiv), Fmoc-His(Trt)-OH (438mg, 4 equiv), Fmoc-Leu-OH (350mg, 4 equiv), Fmoc-Pro-OH (320mg, 4 equiv) were connected to the resin using an analogous synthetic strategy. Following the final removal of the Nα-Fmoc group, the peptide-resin was washed with DMF. The free peptide was obtained by cleavage through the use of 9 mL of TFA in the presence of 750 μL of water and 750 μL of TIPS according to the standard procedure. After cleavage, the peptide was purified by preparative reverse phase

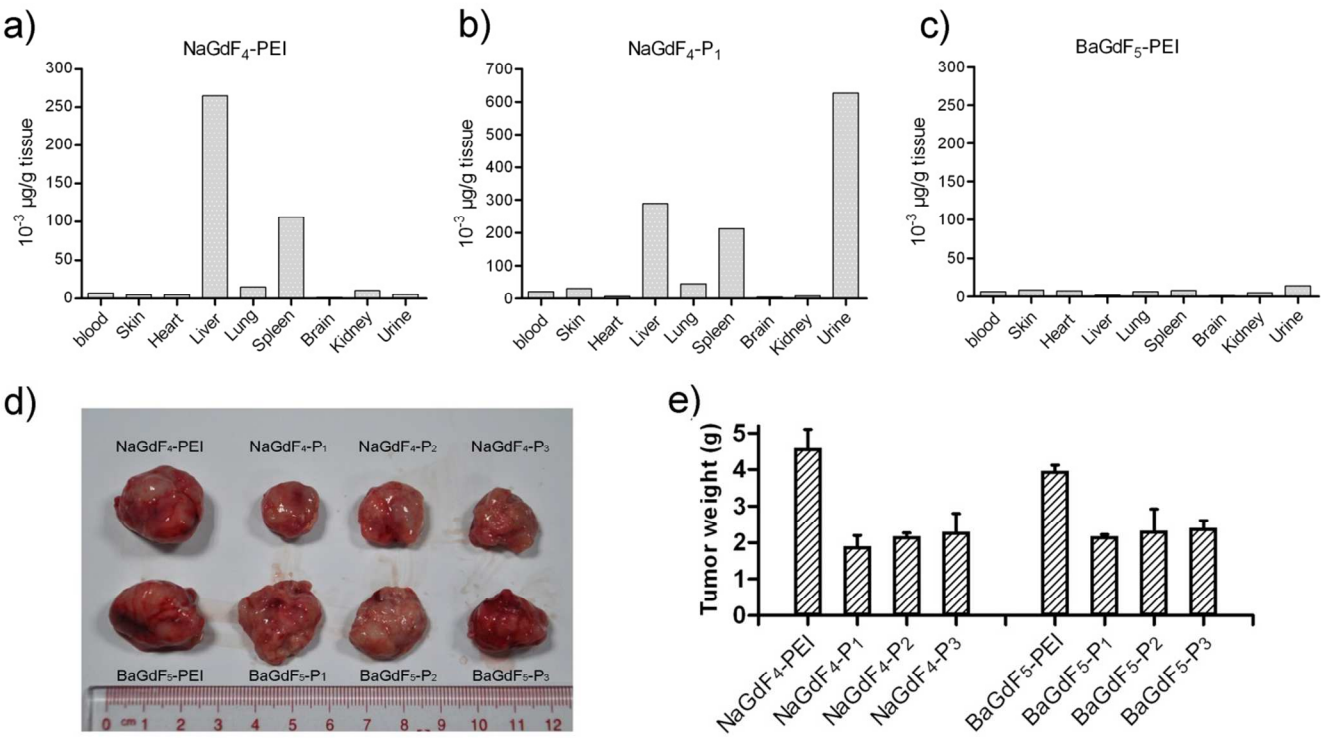

Figure 8. (a) – (c) *in vivo* uptake profiles of **$NaGdF_4$-PEI**, **$NaGdF_4$-P_1** and **$BaGdF_5$-PEI** analyzed by ICP-MS respectively. (d) Tumor inhibition effect of **$NaGdF_4$-P_n and $BaGdF_5$-P_n** via subcutaneous injection around the tumor. (e) Xenograft tumor weight after the treatment of **$NaGdF_4$-P_n and $BaGdF_5$-P_n**.

HPLC. The main peptide-containing fractions were collected and lyophilized. The purity of all final products was confirmed by analytical reverse phase HPLC. **P_2** and **P_3** was obtained and purified by the same methodology as the preparation of **P_1**. **P_1**:**PLHSpT** MALDI-TOF HRMS ($[M+1]^+$, *m/z*): Calcd for $C_{24}H_{42}N_8O_{10}P$, 633.27; found for $[M+H]^+$, 633.26; **P_2**: **PLHSD** MALDI-TOF HRMS ($[M+1]^+$, *m/z*): Calcd for $C_{23}H_{37}N_8O_8$, 568.37; found for $[M+H]^+$, 568.45; **P_3**:**GGPLHSpT**MALDI-TOF HRMS ($[M+1]^+$, *m/z*): Calcd for $C_{28}H_{47}N_{10}O_{12}P$, 746.31; found for $[M+H]^+$ 747.330.

3.4 Bio-conjugation of Plk1 specific peptides onto $NaGdF_4$ or $BaGdF_5$

50 mg PEI **$NaGdF_4$**nanocrystal was added to 744 mg DCC, 200 mg acrylic acid and 266 NHS in DMF to react at room temperature overnight. The excess DCC, acrylic acid and NHS were removed by washing with DMF and methanol. The precipitate was then vacuum dried. 30.8 mg DCC, 15.9 mg NHS and 40 mg 3-(tritylthio) propanoic acid were added to 50mg Plk1 peptide in DMF and stirred at room temperature overnight. Excess DCC, NHS and 3-(tritylthio) propanoic acid were removed by washing with DMF and methanol. The resin of modified Plk1 peptide was removed by reacting with TFA, TIS and De-ionized water in the ratio of 90:5:5 for 4 hours at room temperature. Finally, the modified **$NaGdF_4$** nanocrystal and Plk1 peptide reacted with each other in PBS buffer at pH 7.4 at room temperature overnight. The product was washed with water and methanol for three times and vacuum dried overnight. The bioconjugation of Plk1 specific peptides (**P_n**) onto **$BaGdF_5$** is similar with that of **$NaGdF_4$** but with **$NaGdF_4$** replaced with **$BaGdF_5$**. The characterization of the **$NaGdF_4$-P_n** or **$BaGdF_5$-P_n** was employed with FTIR transmittance and zeta potential analysis.

3.5 Characterization

Powder X-ray diffraction (XRD) patterns of the as-prepared **$NaGdF_4$** or **$BaGdF_5$** and **$NaGdF_4$-P_n** or **$BaGdF_5$-P_n** were recorded using a Rigaku smart lab 9kW (Rigaku Japan) with Cu-Ka radiation (λ= 1.5406Å). The step scan covered the angular range from 25° to 60° in steps of 0.02°. The morphology of the as-prepared samples was characterized by using Tecnai G2 20 S-TWIN Transmission Electron Microscope operated at 200 kV. Fourier transform infrared (FT-IR) spectrometer (Nicolet Avator 630) was used to record infrared spectra of the samples by using KBr pellet technique. The powder materials were pressed into a tungsten mesh grid and installed *in situ* FT-IR transmittance cell, and the samples were degassed in a vacuum system with a residual pressure of less than 3 x 10^{-4} torr at room temperature. UC spectra were recorded using FLS920P Edinburgh analytical instrument apparatus equipped with a 980 nm diode laser as an UC pump source.

3.6 Cell Culture

Human nasopharyngeal carcinoma (HK-1) cells and cervical carcinoma (HeLa) cells were cultured in DMEM medium (Gibco) supplemented with 10% fetal bovine serum (Gibco) and antibiotics (penicillin 50 μg/mL; streptomycin 50 μg/mL).Human liver-derived (QSG-7701) cell were maintained in RPMI 1640 medium supplemented with 10% fetal bovine serum (FBS) and 1% penicillin and streptomycin. Human normal lung fibroblast (MRC-5) cell were grown in MEM

medium supplemented with 10% fetal bovine serum (FBS) and 1% penicillin and streptomycin. All the cells were incubated at 37 ^{o}C in a humidified environment with 5 % CO_2.

3.7 The cellular uptake of $NaGdF_4$-P_n or $BaGdF_5$-P_n by ICP-MS

To measure the intracellular concentration of the **$NaGdF_4$-P_n** or **$BaGdF_5$-P_n**. 1 x 10^5 cells were plated in each well and incubated with the complex for at 100 μg/mL, which was the same as in vitro imaging. After co-incubation, the cell culture medium containing **$NaGdF_4$-P_n** or **$BaGdF_5$-P_n** was removed and the exposed cells were further washed with 1mL PBS for 3 times to remove **$NaGdF_4$-P_n** or **$BaGdF_5$-P_n** adhering to the outer cell membrane and the bottom of the confocal dishes. Then the cells were trypsinized and dispersed into 1mL of culture medium. The exposed cells were collected by centrifugation at 4000 rpm and the cell pellet was digested in 100 μL of concentrated HNO_3 (69%) at 70 ^{o}C for 3 hours. The cellular uptake of **$NaGdF_4$-P_n** or **$BaGdF_5$-P_n** was determined using an Agilent 7500 series of inductively coupled plasma mass spectroscopy (ICP-MS). All ICP experiments were performed in triplicate and values obtained were averaged. The concentration of Gd per cell was calculated by determining the concentration of Gd in the cell lysate by ICP-MS and then dividing it by the number of cells which counted by haematocytometer.

3.8 *In vitro* Bio-imaging

To investigate the suitability of the obtained and Plk1 specific peptides coated UCNPs as bio-probes, imaging of HeLa cells (1 x 10^5) was conducted. After the incubation with **$NaGdF_4$-P_n** or **$BaGdF_5$-P_n** for 24 hours, the cells were washed by PBS for 3 times before imaging. The *in-vitro* imaging was performed on a confocal laser scanning microscope, Leica TCS SP5, equipped with a Ti: Sapphire laser (Libra II, coherent). The samples were excited by a 980nm wavelength laser.

3.9 Plk1 GFP co-staining in vitro Bio-imaging

To validate the binding between **$NaGdF_4$-P_n** or **$BaGdF_5$-P_n** and Plk1, GFP co-staining experiment was carried out. Plk1 full length cDNA was PCR amplified from pOTB7-Plk1 and inserted in to multiple cloning sited (MCS) of pEGFP-C3 (CLONETECH, #6082-1) using restriction digestion sites of XhoI/EcoRI for GFP-Plk1 expression. The positive recombinant was selected through kanamycin proved by sequencing. Plasmids were purified using StarPrep Plasmid Miniprep Kit (Genstar). For transfection, 3.5cm dish of HeLa cells (with 70-80% confluence) were transfected with 8 μg DNA using lipofectamine2000 according to the manufactures. Then, 500 μL of the lipofectamine 2000 and plasmid were added to the confocal dish with 500 μL cell medium. After incubation of 8 hours, 100 μg/mL of **$NaGdF_4$-P_n** or **$BaGdF_5$-P_n** was added and incubated for 24 hours. The imaging procedures and parameters were the same as the previous in vitro bio-imaging section.

3.10 MTT inhibition rate assay

1 x 10^5 of HK-1, HeLa, QSG-7701 and MRC-5 were treated with **$NaGdF_4$-PEI** or **$BaGdF_5$-PEI** and **$NaGdF_4$-P_n** or **$BaGdF_5$-P_n** for 24 hours. Then the cells were treated with nanoparticles at 4 concentrations. (100ug/mL, 50 ug/mL, 20 ug/mL and 5 ug/mL) The cell monolayers were rinsed with phosphate buffer saline (PBS) once and incubated with 0.5mg/mL MTT solution. The cellular inhibitory potency of the nanoparticles were examined by the formation of formazan after addition of MTT (3-(4, 5-dimethylthiazol-2-yl)-2 and 5-diphenyltetrazolium bromide) for 4 hours to allow formazan production during cell metabolism. After that, formazan were fully dissolved in DMSO through oscillating. Finally, the absorbance of solution was measured with Biotek Power wave xsMicroplate Reader at the wavelength of 570nm and 690nm.

3.11 Flow cytometry

10^6 cells were harvested by trypsine digestion, washed twice in PBS, and then fixed in 70% ethanol for 2 hours at 4^{o}C. After removal of the ethanol, cells were resuspended in PBS and then subjected to PI staining (1% triton-100, 50 μg/mL RNase A, 20 μg/mL propidium iodide) for 40 minutes at 37^{o}C. Cell phase distributions were analyzed in BD FACS Calibur and the results were processed by Flowjo 7.6.1, showed as offset histogram and column.

3.12 Antibodies and western blotting

Anti-β-actin (#66009-1-Ig) antibodies were purchased from Proteintech Group, Inc. Anti-CDK1 (#9116) and anti-Plk1 (#4535) antibodies were from Cell Signaling Technology. HeLa cells in 12 well-plate were treated with nanoparticles (1, 10, 50, 100 μg/mL each) for 24 hours, and then rinsed in PBS twice after the culture medium was discarded. Direct lysis in 50mM tris-HCl, pH 6.8, 1% SDS, 10% glycerol and thorough denaturation in boiling water bath were followed. The supernatant was collected as clear lysis after centrifugations. Equal amounts of total proteins were loaded onto the 10% nitrocellular membranes, which was followed by western blotting. All the results finally were analyzed by Gel-Pro analyzer and GraphPad Prism 5 software.

3.13 Pull down assay

Five 10-cm dishes of cells were lysed in RIPA buffer (50mM tris pH=7.4, 150mM NaCl, 1% NP-40, phenylmethanesulfonyl fluoride (PMSF) 1 mM, cocktail protease inhibitors) for 15 minutes on ice, and then centrifuged at 13,000 rpm for 20 minutes. The clear supernatant was collected and the total 5mL cellular lysate was divided to eight samples subject to the incubation with **$NaGdF_4$** or **$BaGdF_5$** nanoparticles series (100 μg each) on 4 ^{o}C for 2 hours. Nanoparticles precipitated proteins were collected by short centrifugation and washed with RIPA buffer for three times to remove unbound proteins. Finally, the pull-down proteins underwent SDS-PAGE separation followed by antibodies detection.

3.14 Animals and ethics

BALB/c nude mice were provided by Guangdong Medical Laboratory Animal Center, with the licensing number of SCXK-2008-0002 approved by Guangdong Science and Technology Department. Mice were kept in the isolated bio-safety facility for specific pathogen-free animals. All animals feeding and experiments were performed according to the Procedures for the Care of Laboratory Animals approved by

Shenzhen Institute of The Hong Kong Polytechnic University (with Use Permit of Experiment Animal license SCXK-2010-0062.

3.15 Mouse xenograft tumor inhibition and ICP-MS bio-distribution analysis

For tumor inhibition assays, human HeLa cells were trypsinized, harvaested and resuspended in DMEM. $1x10^6$ cells in 100 μL DMEM were injected s.c. into the flanks of the mice (6 weeks old). After 14 days when the tumors were about 150 mm^3, the animals were randomized into groups for experiments. **$NaGdF_4$** and **$BaGdF_5$** series of nanoparticles of Plk1 (500 μg for a tumor) were injected around the tumor and kept the mice for another 7 days. Finally, tumors were extracted and imaged. For ICP-MS bio-distribution analysis, 200 μg nanoparticles were i.p. injected into mice, and the tissues as well as urine after 24-hour post-injection were collected. Tissues were digested with nitric acid and subjected to ICP-MS for measuring the concentrations of Gd.

4. Conclusions

Plk1 has emerged as a promising target for the development of new anti-cancer agents. The polo box domain (PBD) of Plk1 provides an excellent target for the development of molecules to inhibit Plk1 activity and as such we have rationally designed multifunctional lanthanide-doped unconverted nanomaterials to exploit this. Specifically our aim was to design novel nanomaterials that could deliver Plk1 specific peptides into cancer cells causing Plk1 inhibition while simultaneously allowing direct NIR imaging and monitoring. $NaGdF_4$: Yb^{3+}, Er^{3+} (**$NaGdF_4$**) and $BaGdF_5$: Yb^{3+}, Er^{3+}(**$BaGdF_5$**) nanoparticles of two different sizes (60 nm and 10 nm, respectively) were prepared and then conjugated with Plk1 specific peptides (**-P_1** = PLHSpT, **-P_2** = PLHSD, and **-P_3** = GGPLHSpT) to generate novel nanomaterials. Systematic and comparative studies of the nanomaterials prepared were carried out with, structural morphology and phase composition, upconversion photophysical properties, cellular uptake efficiency, cytotoxicity, tumor selectivity, and Plk1 binding affinity and inhibitory potency also investigated in detail. The experimental results obtained showed that several of the nanomaterials prepared could achieve our original dual-function aim of anti-cancer activity and NIR imaging. Of the novel bio-conjugated nanomaterials investigated in our study, **$NaGdF_4$-P_1**, demonstrated considerable promise as a system for further development. **$NaGdF_4$–P_1** emerged as the best candidate for Plk1 binding and imaging and it could effectively exert cell cycle G2/M arrest and thus tumor inhibition both *in vitro* and *in vivo*. It is also worth noting that **$NaGdF_4$-P_1** is selective in its mode of action and that no anti-growth effects on the normal cells lines used in this study were observed. In summary, this study represents one of few examples where systems have been developed that are capable of both Plk1 inhibition and simultaneously direct NIR imaging and monitoring of cancer cells.

Acknowledgements

This works was funded by grants from The Hong Kong Research Grants Council (HKBU 203013), ESPRC, Hong Kong Baptist University, The Hong Kong Polytechnic University and Durham University.

Notes and references

[a]Department of Chemistry, Hong Kong Baptist University, Kowloon Tong, Hong Kong.
[b]Department of Applied Biological and Chemical Technology, The Hong Kong Polytechnic University, Hung Hom, Hong Kong.
[c]Department of Chemistry, Durham University, Durham, HK, DH1 3LE.
[d]School of Chemistry and Material Engineering Jiangsu, Key Laboratory of Advanced Functional Materials, Changshu Institute of Technology, Changshu, China
[e]Department of Applied Physics, The Hong Kong Polytechnic University, Hung Hom, Hong Kong
[f]Changshu Research Institute of Hong Kong Baptist University, Changshu Economic and Technological Development Zone, Jiangsu 215500, China.
[g]State Key Laboratory for Chirosciences from The Ministry of Science and Technology of the People's Republic of China, The Hong Kong Polytechnic University, Hung Hom, Hong Kong
Electronic Supplementary Information (ESI) available: [details of any supplementary information available should be included here]. See DOI: 10.1039/b000000x/

1 B. T. Martin, K. Strebhardt; *Cell Cycle*, 2006, 5, 2881.
2 M. A. Van Vugt, R. H. Medema; *Oncogene*, 2005, 24, 2844.
3 X. Liu, M. Lei, R. L. Erikson; *Mol. Cell Biol*, 2006, 26, 2093.
4 B. Vogelstein, N. Papadopoulos, V. E. Velculescu, S. Zhou, L. A. Jr Diaz, K. W. Kinzler;*Science*,2013, 339, 1546.
5 S. M. Lens, E. E. Voest, R. H. Medema; *Nat. Rev. Cancer*, 2010, 10, 825.
6 K. Strebhardt, L. Kneisel, C. Linhart, A. Bernd, R. Kaufmann; *Jama*, 2000, 283, 479.
7 V. Maire, F. Némati, M. Richardson, A. Vincent-Salomon, B. Tesson, G. Rigaill, E. Gravier, B. Marty-Prouvost, L. De Koning, G. Lang, D. Gentien, A. Dumont, E. Barillot, E. Marangoni, D. Decaudin, S. Roman-Roman, A. Pierré , F. Cruzalegui, S. Depil, G. C. Tucker, T. Dubois; *Cancer Res*, 2013, 73, 813.
8 X. Liu, R. L. Erikson; *Proc. Natl. Acad. Sci U S A*, 2003, 100, 5789.
9 R. Lan; G. Lin, F. Yin, J. Xu, X. Zhang, J. Wang, Y. Wang, J. Gong, Y. Ding, Z. Yang, F. Lu, H. Zhang; *Lab Invest.*, 2012, 92, 1503
10 K. V. Gleixner, V. Ferenc, B. Peter, A. Gruze, R. A. Meyer, E. Hadzirjusufovic, S. Cerny-Reiterer, M. Mayerhofer, W. F. Pickl, C. Sillaber, P. Valent; *Cancer Res*, 2010, 70, 1513.
11 J. Q. Shi, K. Lasky, V. Shinde, B. Stringer, M. G. Qian, D. Liao, R. Liu, D. Driscoll, M. T. Nestor, B. S. Amidon, Y. Rao, M. O. Duffey, M. G. Manfredi, T. J. Vos, N. D' Amore, M. L. Hyer; *Mol. Can. Ther.,*2012, 11, 2045.
12 F. Liu, J. E. Park, W. J. Qian, D. Lim, M. Gräber, T. Berg, M. B. Yaffe, K. S. Lee, T. R. Burke Jr; *Nat. Chem. Biol.*, 2011, 9, 595.
13 S. M. Yun, T. Moulaei, D. Lim, J. K. Bang, J. E. Park, S. R. Shenoy, F. Liu, Y. H. Kang, C. Liao, N. K Soung, S. Lee, D. Y. Yoon, Y. Lim, D. H. Lee, A Otaka, E. Appella, J. B. McMahon, M. C. Nicklaus, T. R. Burke Jr, M. B. Yaffe, A. Wlodawer, K. S. Lee; *Nat. Struct. Mol. Biol., 2009,* 16, 876.
14 S. M. Kim, S. Yoon, N. Choi, K. S. Hong, R. N. Murugan, G. Cho and E. K. Ryu;*Biomaterials*, 2012, 33, 6915.
15 I. R. Ruttekolk, F. Duchardt, R. Fischer, K. H. Wiesmuller, J. Rademann, R. Brock; *Bioconjugate Chem*., 2008, 10, 2081.

16 J. Yuan, A. Hoerlin, B. Hock, H. J. Stutte, H. W. Ruebsamen, K. Strebhardt; *Am. J. of Pathol.*, 1997, 4, 1165.
17 Z. H. Chen, R. J. Zhao, R. H. Li, C. P. Guo, G. J. Zhang; *PloS. One*., 2013, 8, e53291.
18 H. Li, C. F. Chan, W. L. Chan, S. Lear, S. L. Cobb, N. Mak, T. C. Lau, R. Lan, W. K. Wong, K. L. Wong, K. L. *Org. Biomol. Chem.*, 2014, 12, 5876
19 X. Xie, N. Gao, R. Deng, Q. Sun, Q. H. Xu, X. Liu; *J. Am. Chem. Soc*., 2013, 34, 12608.
20 Y. F. Wang, G. Y. Liu, L. D. Sun, J. W. Xiao, J. C. Zhou, C. H. Yan; *ACS Nano*, 2013, 8, 7200.
21 P. Escribano, B. Julian-Lopez, J. Planelles-Arago, E. Cordoncillo, B. Viana, C. Sanchez, *J. Mat. Chem*., 2008, 18, 23
22 S. Zeng, M. K. Tsang, C. F. Chan, K. L. Wong, J. Hao; *Biomaterials*, 2012, 33, 9232.
23 R. Naccache, P. Chevallier, J. Lagueux, Y. Gossuin, S. Laurent, L. Vander Elst, C. Chilian, J. A. Capobianco, M. A. Fortin; *Adv. Health. Mat.*, 2013, 2, 1478
24 N. Bogdan, E. Martín Rodríguez, F. Sanz-Rodríguez, M. C. Iglesias-de la Cruz, A. Juarranz de la Fuente, D. Jaque, J. GarcíaSolé, J. A. Capobianco; *Nanoscale*, 2012, 4; 3647
25 Q. Liu, W. Feng, T. Yang, T. Yi, F. Li, F. *Nat. Prot.,* 2013, 8, 2033
26 W. Feng, C. Han F. Li; *Adv. Mat.,* 2013, 25, 5287
27 L. D. Carlos, R. A. S. Ferreira, V. Z. Bermudez, B. Julian-Lopez, P. Escribano; *Chem. Soc. Rev.,* 2011, 40, 536
28 M. L. Debasu, D. Ananias, S. L. C. Pinho, C. F. G. C. Geraldes, L. D. Carlos, J. Rocha; *Nanoscale,* 2012, 4, 5154
29 J. Wu, Q. Tian, H. Hu, Q. Xia, Y. Zou, F. Li, T. Yi, C. Huang; *Chem. Comm.,* 2009, 27, 4100
30 Q. Liu, B. Yin, T. Yang, Y. Yang, Z. Shen, P. Yao, F. Li; *J. Am. Chem. Soc*., 2013, 13, 5029.
31 S. J. Butler and D. Parker; *Chem. Soc. Rev*., 2013, 42, 1652.
32 C. F. Chan, M. K. Tsang, H. Li, R. Lan, F. L. Chadbourne, W. L. Chan, G. L. Law, S. L. Cobb, J. Hao, W. T. Wong, K. L. Wong, *J.Mat. Chem. B*, 2014, 2, 84.
33 P. Loyera, J. H. Trembleya, R. Katonac, V. J. Kidda, J. M. Lahti;*Cellular Signalling*, 2005, 17, 1033.
34 E. Pretsch, P. B¨uhlmann and C. Affolter; *Structure Determination of Organic Compounds*, Springer, Berlin Heidelberg, 2000, p. 250.

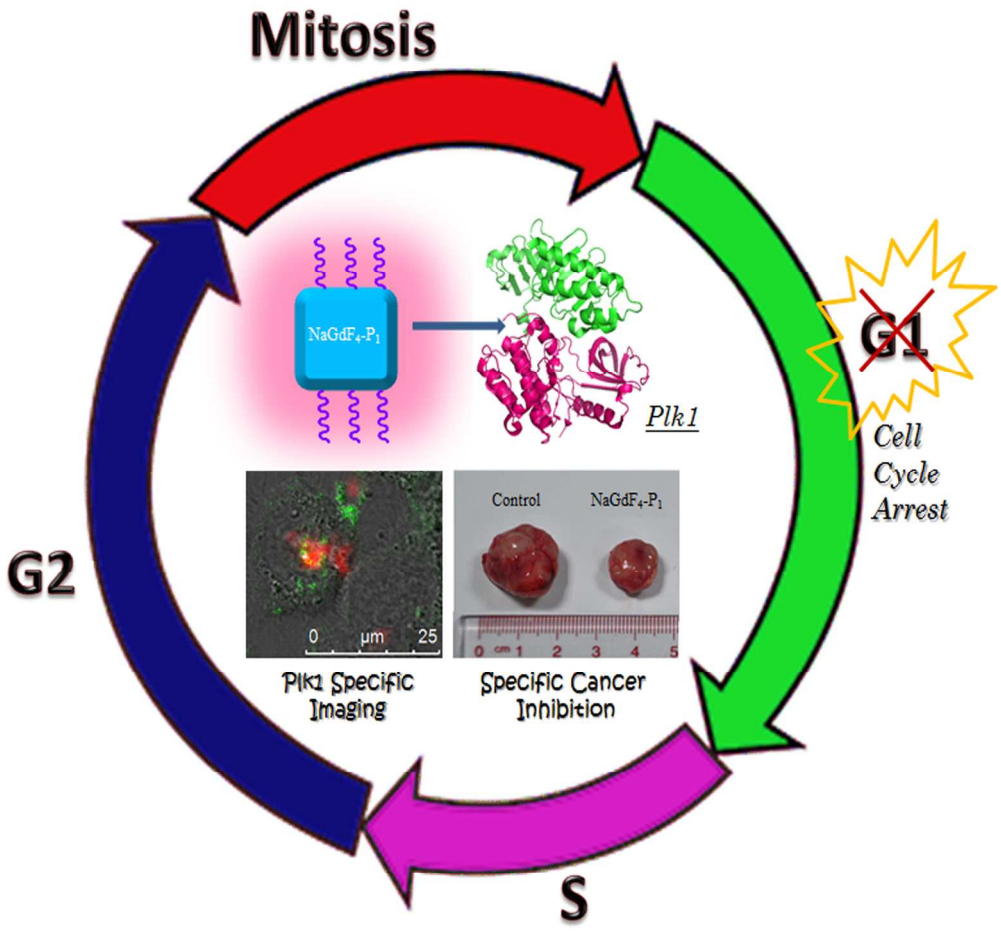

211x211mm (300 x 300 DPI)